

# Dense and Warm Molecular Gas in Arp 220

Jun-Hui Zhao\* and Tao An†

\*Harvard-Smithsonian Center for Astrophysics, 60 Garden Street, MS 78, Cambridge, MA 02138

†Shanghai Astronomical Observatory, Chinese Academy of Sciences, Shanghai 200030, P. R. China

**Abstract.** We present the results from the observations of Arp 220 in multiple CO spectral line transitions of  $J=6-5$ ,  $J=3-2$ ,  $J=2-1$  and the isotope  $^{13}\text{CO}$  at  $J=2-1$  at 690, 340 and 230 GHz using the Submillimeter Array (SMA) with the angular resolutions of sub-arcsec to a few arcsec. Based on the measured line ratios, we modeled the excitation conditions of the molecular clouds in the nuclear region of Arp 220, suggesting that the CO  $J=6-5$  emission arises from dense ( $n(\text{H}_2) \sim 10^5 \text{ cm}^{-3}$ ) and warm ( $T_k \sim 60 \text{ K}$ ) cloud components. Each of the four CO  $J=6-5$  clumps contains at least a few times  $10^8 M_\odot$  molecular gas. The dense and warm molecular clouds are likely the consequence of inelastic collisions between the molecular clouds in the counterrotating nuclear disks. Properties determined from these high-density regions suggest that they are in the early stage of star formation. The study of Arp 220 could provide us detailed information on the astrophysical processes in the galaxies at high redshifts.

**Keywords:** Submillimeter, Molecular clouds, Galaxy mergers

**PACS:** 95.85.Fm, 98.58.Db, 98.65

## INTRODUCTION

Arp 220 is the prototypical ultra-luminous infrared galaxy (ULIRG) [22, 23]. This galaxy is believed to be in the final stage of galactic merging [2, 12, 14, 9]. The radio and infrared (IR) continuum emission is concentrated in two compact components (Arp 220E and Arp 220W) with a separation of  $\sim 1''$  [14, 3, 9, 5, 17]. The CO line observations suggested that a large fraction of molecular gas ( $M_{\text{H}_2} \sim 10^{10} M_\odot$ ) is concentrated in the inner  $\sim 500$  pc of the nuclear region [19, 20]. The molecular gas concentration and the enormous FIR luminosity in the nuclear region of Arp 220 were suggested to be the consequence of starbursts driven by the merging process. Because of its proximity ( $D = 77$  Mpc), Arp 220 provides an excellent case for us to study the starburst process under extreme astrophysical circumstances. Arp 220 is a template for studying the formation of the first generation stars in high redshift galaxies.

Carbon monoxide (CO) is one of the major coolants in molecular clouds. Analysis of multiple-line CO emission suggests that higher-J CO lines (CO( $J=5-4$ ) and above) account for the major cooling in starburst nuclei[4]. For example, the CO SEDs in nearby starburst galaxies M 82 and NGC 253 peak at ( $J=7-6$ ) and ( $J=6-5$ ) transitions, respectively[11]. Observations of high density tracers in ULIRGs indicate that a large fraction of gas is probably in dense phase in the starburst nuclei. Therefore observations of higher-J CO transitions are critical to determine the physical conditions of molecular gas in the starburst nuclei. Given the upper level energy of 116 K above the ground and the critical density of  $10^6 \text{ cm}^{-3}$ , CO ( $J=6-5$ ) is an excellent probe to the warm and dense molecular

clouds.

## OBSERVATIONS

The observations of Arp 220 were carried out simultaneously in the two receiver bands of 230 and 690 GHz using the SMA in its compact array configuration with angular resolutions of  $3''$  and  $1''$ . The observations covered the CO ( $J=6-5$ ), ( $J=2-1$ ) and  $^{13}\text{CO}$  ( $J=2-1$ ) at the rest frequencies of 691.473, 230.538 and 220.399 GHz respectively. In addition, CO ( $J=3-2$ ) was also observed with the SMA in the compact and very extended array configurations, which gives the angular resolution of  $1''$ . Arp 220 was the first target for the SMA to observe the high transition CO at submillimeter wavelengths.

The data reduction was carried out with the Miriad package<sup>1</sup>. Ceres (at 203/690 GHz) and Uranus (at 340 GHz) were used to determine the flux density scale. For the 230 and 340 GHz data, the standard calibration procedure was used to correct for the atmosphere attenuation, bandpass shape and complex gains. For the 690 GHz data, two methods were used in the initial calibration for phase: (1) phase transfer and (2) the standard phase reference techniques. Then the residual errors were corrected with the self-calibration technique using the clean component model derived from the data initially calibrated with either phase transfer or the standard phasae reference techniques. The final maps of Arp 220 derived from the two methods were compared. In both

<sup>1</sup> <http://smadata.cfa.harvard.edu/miriadWWW/>

methods, the positions of the two continuum peaks at 690 GHz are coincident with the radio positions[1, 16] in an uncertainty of  $0.1''$ .

## RESULTS

### The brightest CO component

Figure 1 shows the spectra of the brightest CO region in Arp 220. Each of the spectra shows more than one components in velocity. We fitted multiple Gaussians to the spectra and listed the properties of the brightest CO component (Table 1). At CO ( $J=6-5$ ) transition, the spectrum peaks at  $5341 \pm 40$  km s $^{-1}$  with FWHM of  $183 \pm 5$  km s $^{-1}$  and the position of this component appears to be offset significantly from the west component of the double nuclear continuum source ( $\Delta\alpha_{J2000} = 0.21 \pm 0.07$ ,  $\Delta\beta_{J2000} = -0.35 \pm 0.07$ ).

The peak in the CO ( $J=6-5$ ) spectrum is at  $\sim 5400$  km s $^{-1}$ , and a secondary peak is at  $\sim 5600$  km s $^{-1}$ . The primary peak in the CO ( $J=6-5$ ) spectrum is more prominent as compared to those in the spectra of lower- $J$  CO transitions. The gas component at  $\sim 5400$  km s $^{-1}$  appears to be highly excited in CO ( $J=6-5$ ), suggesting presence of a warm and high density component in Arp 220.

### CO ( $J=6-5$ )

Figure 2 shows the integrated intensity map of the CO ( $J=6-5$ ) (color) overlaid on the continuum map (contours). The CO ( $J=6-5$ ) emission appears to arise from a few clumps. There is no significant extended diffuse (angular size  $> 1''$ ) line emission in CO ( $J=6-5$ ). The morphology and distribution are consistent with the fact that the CO ( $J=6-5$ ) traces the warm, high density molecular gas located in the nuclear region. The warm, high density gas appears to concentrate in the inner  $2''$  region, showing four major clumps with typical angular size of  $1''$ .

Figure 2 also shows the structure of the double component in continuum at 690 GHz (0.43 mm) agrees well with the sub-arcsec resolution observations at radio, mm and NIR wavelengths [14, 9, 3, 5, 17]. Most of the dust continuum emission is concentrated in the two compact components. The western component (Arp 220W) appears to be much stronger. The peaks of the dust emission are consistent with the radio positions [1, 16]. CO( $J=6-5$ ) line emission appears to be significantly offset from the continuum positions, suggesting that the excitation condition of CO ( $J=6-5$ ) emission gas differs from that of the lower- $J$  CO gas. The position of the brightest component appears to be  $\sim 0.4''$  SE to Arp 220W. A weak

radio component 'C' in the 8.3 GHz radio map [3] and a compact NIR component 'S' [21] are found in the vicinity of the CO ( $J=6-5$ ) line peak. However, it is difficult to accurately determine the position of IR sources due to the complex of source structure and the poor coordinate registration in the IR observations.

### CO ( $J=3-2$ )

Figure 3 (left) shows the integrated intensity map of CO ( $J=3-2$ ) line emission or the moment 0 map. The CO ( $J=3-2$ ) emission was integrated with a cutoff of  $5\sigma$  ( $1\sigma=0.035$  Jy) over the line range 5000-6000 km s $^{-1}$ . The integrated flux is  $2980 \pm 600$  Jy km s $^{-1}$ . The uncertainty is dominated by the error in the calibration of flux density scale. The measurement of the CO ( $J=3-2$ ) integrated flux is in excellent agreement with the recent JCMT observations [10]. We note that the CO ( $J=3-2$ ) peak is offset by  $0.3''$  SE to the Arp 220W. Compared to the CO ( $J=6-5$ ) (Figure 2), the CO ( $J=3-2$ ) line emission is more extended, which is consistent with the nature that CO ( $J=3-2$ ) traces relatively lower-density gas. Most of the CO ( $J=3-2$ ) line emission is concentrated in the inner  $4'' \times 4''$  region, showing a bar-like distribution in NE-SW. There is a tail-like structure ( $\sim 5''$ ) extended in the south to Arp 220W. This extended structure was also observed in the CO ( $J=1-0$ ) and ( $J=2-1$ ) transitions in the same direction [20, 5]. The outer part of the tail is located along the dust lane[21].

Figure 3 (right) shows the color-coded map of the CO ( $J=3-2$ ) intensity weighted mean velocity, or a moment 1 map corresponding to the moment 0 map (Figure 3). The general velocity gradient is along the NE-SW direction. With respect to the system velocity of 5450 km s $^{-1}$  of Arp 220, the blue-shifted emission is located in SW and red-shifted in NE, which agrees with that observed in the observations of the lower- $J$  CO emission[20, 5].

### Line intensity ratios

Ratios of integrated intensity between different line transitions and isotope ratio are important in determination of the excitation condition and physical properties of the molecular clouds. From the existing SMA data, we can determine the line-intensity ratios of CO( $J=6-5$ )/CO( $J=3-2$ ) and  $^{12}\text{CO}(J=2-1)$ / $^{13}\text{CO}(J=2-1)$ .

#### *Ratio CO( $J=6-5$ )/CO( $J=3-2$ )*

Figure 4 shows the channel maps of CO ( $J=6-5$ ) (pseudo-color) overlaid on the CO ( $J=3-2$ ) emission

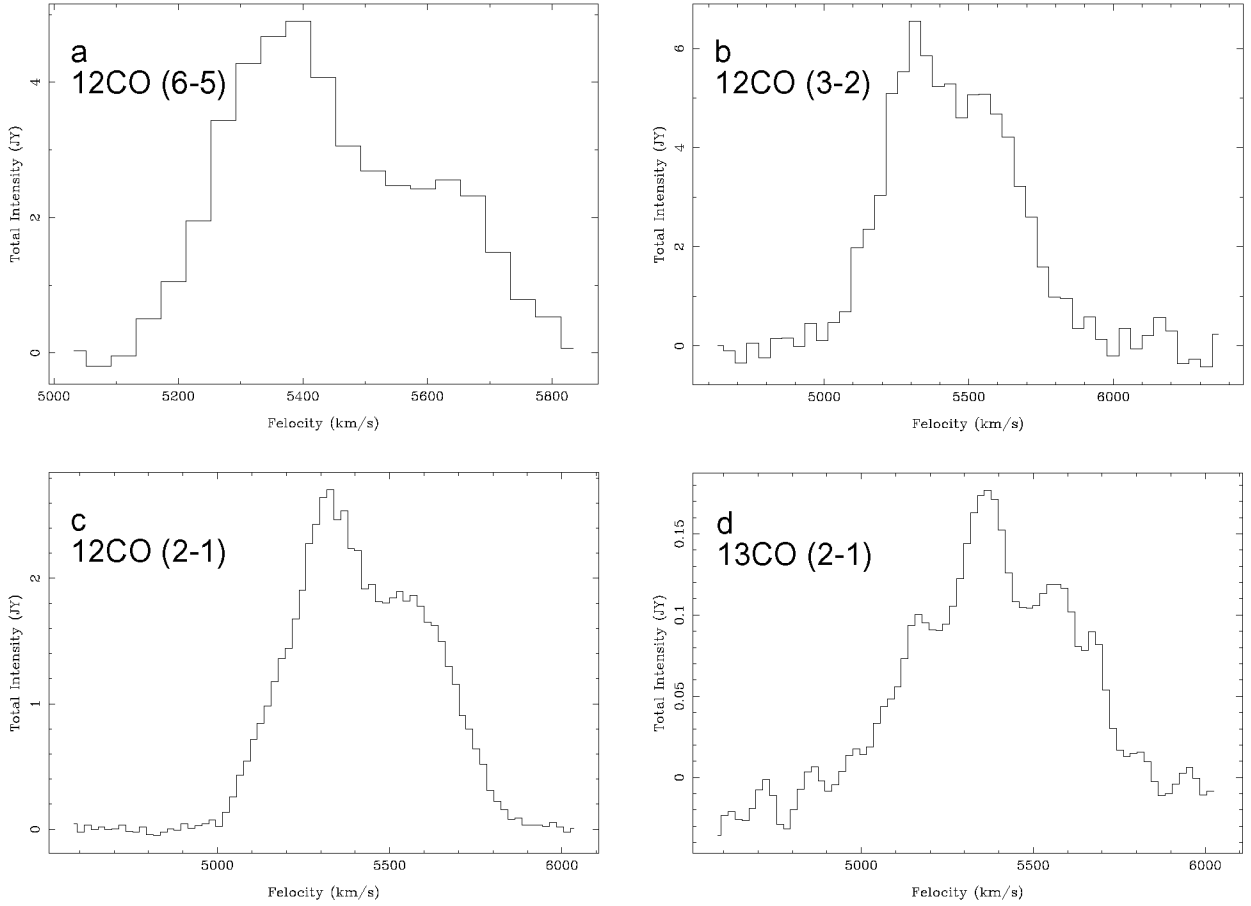


**FIGURE 1.** CO spectra of Arp 220. The CO ( $J=6-5$ ) and ( $J=3-2$ ) emission were binned in  $40 \text{ km s}^{-1}$ , and CO ( $J=2-1$ ) and  $^{13}\text{CO}$  ( $J=2-1$ ) were binned in  $20 \text{ km s}^{-1}$ .

(contours). The CO ( $J=3-2$ ) data were mapped using visibilities on  $uv > 30k\lambda$ , the same cutoff in the uv range of the CO ( $J=6-5$ ) data. The extended emission with angular size greater than  $3''$  was excluded. The CO ( $J=3-2$ ) images were made with the same velocity range with CO ( $J=6-5$ ). The CO ( $J=6-5$ ) emission shows a clumpy distribution but concentrated  $\sim 0.4''$  SE to Arp 220W peaking in  $5354\text{-}5394 \text{ km s}^{-1}$ . The size of this CO ( $J=6-5$ ) concentration is  $1''\text{-}2''$ . The CO ( $J=3-2$ ) also shows a concentration near the CO ( $J=6-5$ ) maximum. The maximum intensity ratio  $\text{CO}(J=6-5)/\text{CO}(J=3-2)$  is  $\sim 2.5 \pm 0.6$ . A red-shifted line emission peaks at  $5630 \text{ km s}^{-1}$  channel, located  $0.3''$  north to Arp 220E, close to the northeast component in the NIR image [21]. There is a good correlation between CO ( $J=6-5$ ) and CO( $J=3-2$ ) in the two major CO ( $J=6-5$ ) concentrations. However, the comparison between the CO ( $J=6-5$ ) and ( $J=3-2$ ) channel maps shows different distribution in details. The CO ( $J=3-2$ ) emission extends to a larger region while CO( $J=6-5$ ) concentrated near the double-nuclei Arp 220W and

Arp 220E. The difference in the distribution between CO ( $J=6-5$ ) and CO ( $J=3-2$ ) reflects that they are sensitive to different gas excitation conditions in different molecular cloud components. The optically thin CO ( $J=6-5$ ) line is better to trace the high-density, warm molecular cloud while the CO ( $J=3-2$ ) line is more sensitive to the diffuse/extended emission.

Figure 5 shows the integrated-intensity ratio (pseudo-color map) of CO ( $J=6-5$ ) to CO ( $J=3-2$ ). The ratio map is overlaid on CO ( $J=3-2$ ) contour map. The three major CO ( $J=6-5$ ) components Arp 220S, Arp 220W and Arp 220 NE stand out clearly in the ratio map, with the integrated line intensity ratio of  $R[\text{CO}(J=6-5)/\text{CO}(J=3-2)] = 2.1 \pm 0.5$ ,  $1.8 \pm 0.4$  and  $1.6 \pm 0.4$ , respectively. The radio continuum source Arp 220E has a lower value of  $R[\text{CO}(J=6-5)/\text{CO}(J=3-2)] = 1.5 \pm 0.4$ , similar with the averaged ratio over the source. The regions with high ratio of CO( $J=6-5$ )/CO( $J=3-2$ ) appears to have their near-IR counterparts[21]. The peak of the eastern H $53\alpha$  emission source appears to be located between CO ( $J=6-5$ )

**TABLE 1.** Measurements of CO lines

Parameters		Measurements		
Transitions . . . . .	CO(J=6–5)	CO(J=3–2)	CO(J=2–1)	$^{13}\text{CO}(J=2–1)$
Properties of the bright spectral component:				
FWHM Beam( $\theta_{maj}'' \times \theta_{min}''$ ) . . .	$1'' \times 1''$	$1'' \times 1''$	$3'' \times 3''$	$3'' \times 3''$
Peak $T_b(\text{K})$ . . . . .	$9.0 \pm 2.3$	$16.7 \pm 3.3$	$5.4 \pm 0.5$	$0.26 \pm 0.03$
Peak $V_{\text{lsr}} (\text{km s}^{-1})$ . . . . .	$5341 \pm 40$	$5314 \pm 40$	$5306 \pm 20$	$5368 \pm 20$
$\Delta V_{\text{FWHM}} (\text{km s}^{-1})$ . . . . .	$183 \pm 5$	$227 \pm 2$	$256 \pm 2$	$150 \pm 11$
$\Delta \alpha_{J2000}^*$ . . . . .	$0.21 \pm 0.07$	$0.08 \pm 0.06$	$-0.11 \pm 0.11$	$0.09 \pm 0.15$
$\Delta \delta_{J2000}^{\dagger}$ . . . . .	$-0.35 \pm 0.07$	$-0.52 \pm 0.05$	$-0.49 \pm 0.11$	$-0.35 \pm 0.14$
$R_p^{**}$ . . . . .		$2.1 \pm 0.5$		$20.5 \pm 4.1$
Properties of the overall source:				
Angular Size ( $\theta_{maj}'' \times \theta_{min}''$ , PA)	$2.4'' \times 2.0'', -20^\circ$	$5.0'' \times 3.8'', 45^\circ$	$11.0'' \times 7.5'', 50^\circ$	$5.5'' \times 4.2'', -30^\circ$
CO Flux ( $10^3 \text{ Jy km s}^{-1}$ ) . . . . .	$1.75 \pm 0.44$	$2.98 \pm 0.60$	$1.39 \pm 0.14$	$0.092 \pm 0.014$
$\Delta \alpha_{J2000}^{\ddagger}$ . . . . .	$0.21 \pm 0.13$	$0.26 \pm 0.11$	$0.11 \pm 0.10$	$0.33 \pm 0.14$
$\Delta \delta_{J2000}^{\$}$ . . . . .	$-0.22 \pm 0.14$	$-0.14 \pm 0.10$	$-0.12 \pm 0.10$	$-0.09 \pm 0.14$
$R_m^{\ \!  }$ . . . . .		$1.5 \pm 0.4$		$15.0 \pm 3.0$

\* Positions of the brightest spectral component, offset from Arp 220W  $\alpha_{2000} = 15^h 34^m 57^s.22$

† Positions of the brightest spectral component, offset from Arp 220W  $\delta_{2000} = 23^\circ 30' 11''$

\*\*  $R_p$  is the peak value of the line-intensity ratio CO(J=6–5)/CO(J=3–2) or CO(J=2–1)/ $^{13}\text{CO}(J=2–1)$ .

‡ Positions of the peak integrated line flux in the moment 0 maps, offset from Arp 220W  $\alpha_{2000} = 15^h 34^m 57^s.22$

§ Positions of the peak integrated line flux in the moment 0 maps, offset from Arp 220W  $\delta_{2000} = 23^\circ 30' 11''.5$

¶  $R_m$  is the mean value of the line-intensity ratio CO(J=6–5)/CO(J=3–2) or CO(J=2–1)/ $^{13}\text{CO}(J=2–1)$

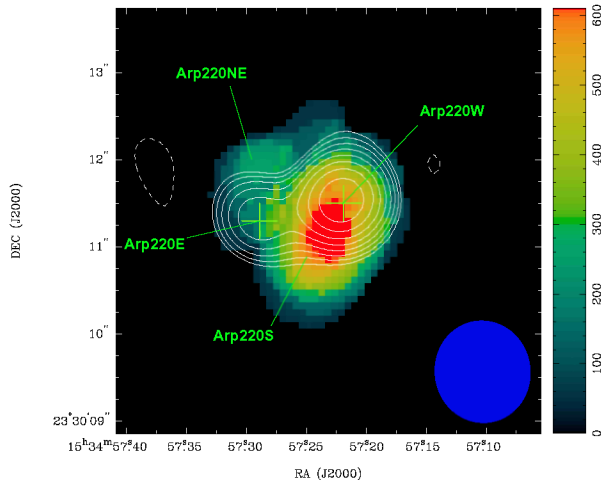


**FIGURE 2.** Integrated CO (J=6–5) line emission (color scale) and continuum emission (contours) from Arp 220. The synthesized beam of the CO (J=6–5) image is  $1.17'' \times 1.09''$ , PA= $8.2^\circ$ , shown in the bottom right corner. The integrated line intensity is scaled in the range  $0$ – $620 \text{ Jy beam}^{-1} \text{ km s}^{-1}$ . The two crosses mark the locations of the radio continuum double nuclei [1, 16]. The size of the crosses is  $0.2''$ , which represents 2 times the astrometry uncertainty at 690 GHz. The map of the continuum emission (contour plot) was made from the line-free channels of the same data set as that of the CO (J=6–5) line, which was restored with a ‘super-resolution’ of  $0.7'' \times 0.7''$ . Both line and continuum data were calibrated in the same calibration manner. The lowest contour is  $0.1 \text{ Jy beam}^{-1}$  ( $4\sigma$ ), and the contours are increased by  $\sqrt{2}$ .

sources Arp 220E and Arp 220NE while the peak of the west H53 $\alpha$  source is located between Arp 220W and Arp 220S. The offsets ( $> 0.3''$ ) in position (more than  $3\sigma$ ) between the CO (J=6–5) emission and the radio continuum sources as well as the H53 $\alpha$  sources appear to be significant.

The observed variation in the line ratio CO(J=6–5)/CO(J=3–2) suggests the excitation condition changes in these nuclear clouds. Similar variations in CO line ratio has also been observed in the nearby starbursts galaxy M82[15] and NGC 253.

$$\text{Ratio } {}^{12}\text{CO}(J=2–1)/{}^{13}\text{CO}(J=2–1)$$

The isotope ratio of  ${}^{12}\text{CO}(J=2–1)/{}^{13}\text{CO}(J=2–1)$  was derived from the same procedure. The mean value of the CO isotope ratio  ${}^{12}\text{CO}(J=2–1)/{}^{13}\text{CO}(J=2–1)$  is  $15 \pm 3$  in Arp 220. The observed maximum of the CO isotope ratio appears to be located at Arp 220E. The difference in the CO isotope ratio is more likely due to the optical depth effect rather than a difference in true CO isotope abundance, suggesting that the optical depth of  ${}^{12}\text{CO}(J=2–1)$  towards Arp 220E is less than that of Arp 220W.

## EXCITATION CONDITIONS

The detection of CO (J=6–5) line emission from a number of super molecular clouds in Arp 220 suggests the

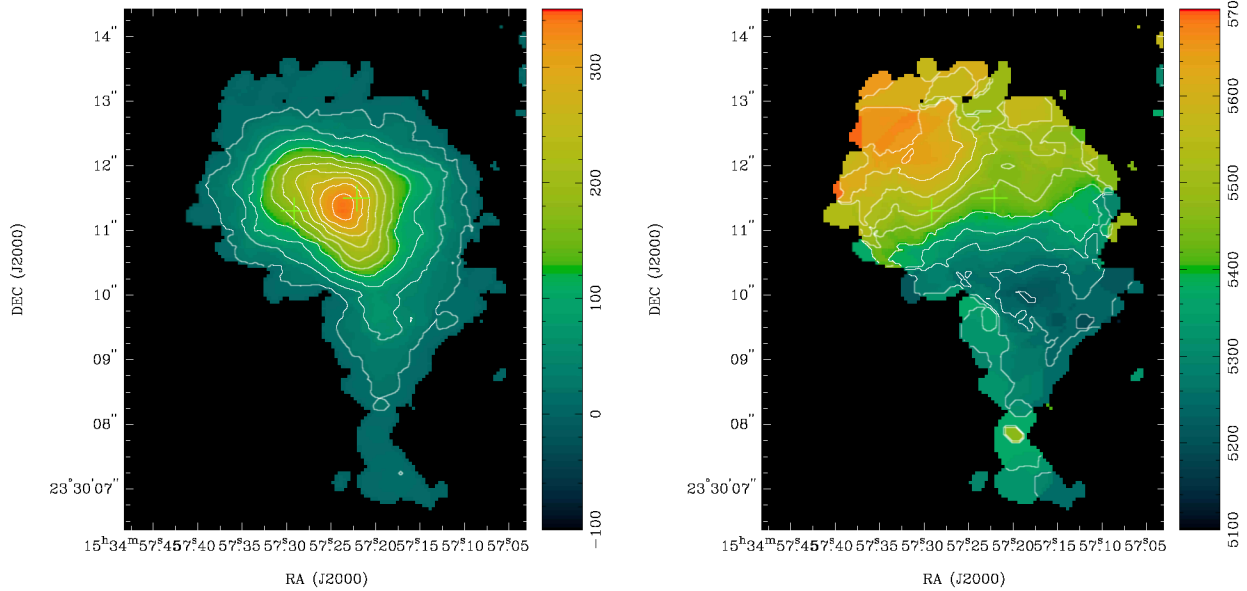


**FIGURE 3.** Left: The map of integrated CO ( $J=3-2$ ) line emission from Arp 220. The image was restored with a  $0.82'' \times 0.65''$  beam (P.A.= $-60.9^\circ$ ), shown in the bottom right corner. The grey scale ranges from 0 to  $520 \text{ Jy beam}^{-1} \text{ km s}^{-1}$ . The two crosses mark the locations of the radio continuum double nuclei [1, 16]. The size of the crosses is  $0.2''$ , corresponding to 2 times the astrometry uncertainty at 340 GHz. The contours are  $10 \times (1, 2, 5, 10, 15, 20, 25, 30, 35, 40, 45, 50, 55)$   $\text{Jy km s}^{-1}$ . Right: The map of intensity-weighted velocity constructed from CO ( $J=3-2$ ) line cube. The contours are spaced by  $40 \text{ km s}^{-1}$ .

existence of a large bulk of warm and dense gas in the nuclear region. In order to constrain the excitation condition of the molecular gas, we solved for the radiation transfer in a multi-level system with the large velocity gradient (LVG) approximation. The escape probability  $\beta = (1 - e^{-\tau})/\tau$  for spherical, gravitational collapsing clouds[8] was used to account for photon trapping. The LVG model calculates intensities of rotational CO lines given a molecular volume density  $n(\text{H}_2)$ , a kinetic temperature  $T_k$ , and a velocity gradient  $dv/dz$ . With the line ratio of  $^{12}\text{CO}(J=2-1)/^{13}\text{CO}(J=2-1)$ , the column density per unit velocity interval ( $N_{\text{CO}}/\Delta v$ ) can be constrained.

The LVG code handles an homogeneous cloud with a uniform density. In the reality, the emission towards the nuclear region is mixed with multiple phases of gas as has been indicated from previous observations[24, 20, 5, 10]. The CO ( $J=3-2$ ) traces the molecular clouds with intermediate density while CO ( $J=6-5$ ) is sensitive to the high density gas. The mean integrated intensity ratio CO( $J=6-5$ )/CO( $J=3-2$ ) of 1.5 determined from the integrated line emission of the overall gas in the nuclear region of Arp 220 reflects the intermediate density component. The true ratio of the high-density component might exceed the maximum ratio of 2.5. Therefore, we treated separately the LVG calculations of CO ( $J=6-5$ ), ( $J=3-2$ ), ( $J=2-1$ ) and  $^{13}\text{CO}$  ( $J=2-1$ ) lines in Arp 220 with two density gas components: an intermediate density component with  $10^4 \text{ cm}^{-3} \geq n(\text{H}_2) \geq 10^3 \text{ cm}^{-3}$  with relatively large volume filling factor ( $f_V \sim 0.1$ ), and a high density

component with  $10^6 \geq n(\text{H}_2) \geq 10^4 \text{ cm}^{-3}$  with a small filling factor ( $f_V \sim 0.01$ ).

We carried out the LVG calculations using the radiative transfer codes developed in Miriad. The LVG model is implemented with the collision rates para-H<sub>2</sub> with CO[6], increased by 21% to account for collisions with helium[13, 18]. In addition, the volume filling factor ( $f_V$ ) assumed for the gas components with different densities in a cluster of giant molecular clouds is incorporated into the optical depth calculation :

$$\tau_0 = \frac{A_{21}c}{8\pi\nu^3} \frac{X_{\text{CO}}(n(\text{H}_2)f_V)}{dv/dz} (x_1 \frac{g_2}{g_1} - x_2) \quad (1)$$

where  $\tau_0$  is the optical depth at the line center,  $A_{21}$  is the Einstein coefficient for spontaneous emission,  $n(\text{H}_2)$  is H<sub>2</sub> density,  $X_{\text{CO}}$  is CO abundance,  $dv/dz$  is the velocity gradient, and  $x_i$  and  $g_i$  are the fractional population and statistical weight of level  $i$ , respectively. The CO abundance ratio  $X_{\text{CO}}$  is assumed to be  $1 \times 10^{-4}$ , a value determined from the galactic molecular clouds[7]. The LVG model directly yields column density per unit velocity interval (or the opacity parameter) at the line center

$$N_{\text{CO}}/\Delta v_{\text{FWHM}} = \sqrt{\frac{\pi}{4\ln(2)}} X_{\text{CO}} n(\text{H}_2) f_V (dv/dz)^{-1}. \quad (2)$$

The actual column density of CO can be determined by multiplying  $N_{\text{CO}}/\Delta v_{\text{FWHM}}$  with the observed FWHM of the line width.

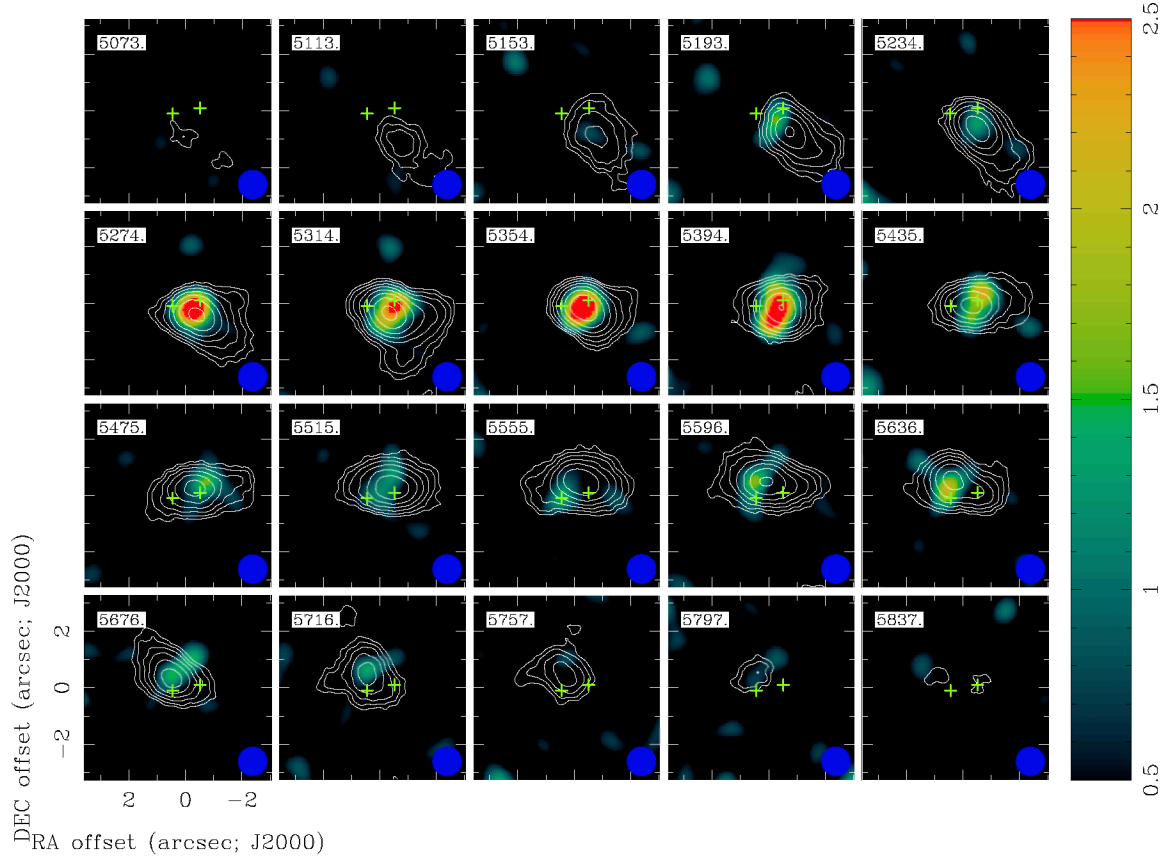


**FIGURE 4.** Channel maps for the  $^{12}\text{CO}$   $J=6-5$  (color scale) and  $^{12}\text{CO}$   $J=3-2$  (contours) line emission shown with velocity resolution of  $40 \text{ km s}^{-1}$ . In each panel, the number indicates the center velocity in  $\text{km s}^{-1}$ . The restoring beam  $1'' \times 1''$  is shown in the bottom right of each panel. The  $^{12}\text{CO}$   $J=3-2$  line emission was derived from the same  $uv$  spacing with the  $J=6-5$  line emission and has been smoothed with a  $40 \text{ km s}^{-1}$  velocity resolution. The grey scale ranges from 0.5 to  $2.5 \text{ Jy beam}^{-1}$ ; the lowest contour is  $0.14 \text{ Jy beam}^{-1}$  ( $4\sigma$ ), increasing with  $\sqrt{2}$ .

From the moment 0 map (Figure 2), the CO ( $J=6-5$ ) emitting gas is concentrated in a number of clumps in the nuclear region. In this paper, we show the calculations for the high-density gas component ( $10^5 > n(\text{H}_2) > 10^4 \text{ cm}^{-3}$ ) assuming the volume filling factors of  $f_V = 0.01$  for CO ( $J=6-5$ ) and 0.1 for the lower- $J$  CO transitions. The model searches in density range  $n(\text{H}_2) = 10^3 - 10^7 \text{ cm}^{-3}$ , and kinetic temperature range  $10\text{K} < T_k < 400\text{K}$ . Figure 6 shows the results of LVG calculations for the high density gas component assuming the velocity gradient of  $dv/dz = 5.0 \text{ km s}^{-1} \text{ pc}^{-1}$ . The dashed curves are the observed curves for the intensity ratios of  $\text{CO}(J=6-5)/\text{CO}(J=3-2)$  and the  $^{12}\text{CO}/^{13}\text{CO}$  at  $J=2-1$ . Since the observed values include the contribution of the extended lower density components, the true ratios to the high density components should be higher than the observed values. Assuming that in both  $\text{CO}(J=6-5)$  and  $\text{CO}(J=2-1)$ , the net contributions to the observed line emission intensities from the high density component were the same as those from the in-

termediate density component, the correction factors to the line ratios of  $\text{CO}(J=6-5)/\text{CO}(J=3-2)$  and  $^{12}\text{CO}(J=2-1)/^{13}\text{CO}(J=2-1)$  would be 1.67 and 1.58. Then the corrected ratios would be  $R[\text{CO}(J=6-5)/\text{CO}(J=3-2)] = 3.5$  and  $R[^{12}\text{CO}(J=2-1)/^{13}\text{CO}(J=2-1)] = 32.4$ , respectively, which are denoted as the thick lines in Figure 6. Then, in Figure 6, the hatched region within the boundaries constrained by the observations corresponds to the solutions for the excitation condition, *i.e.*  $T_k = 58 \pm 20 \text{ K}$  and  $n(\text{H}_2) = 1.5 \pm 1.0 \times 10^5 \text{ cm}^{-3}$ . The CO column density at the line center is  $9.7 \pm 6.5 \times 10^{16} \text{ cm}^{-2} (\text{km s}^{-1})^{-1}$  corresponding to the  $\text{H}_2$  column density of  $1.9 \pm 1.3 \times 10^{23} \text{ cm}^{-2}$  assuming  $\Delta v_{\text{FWHM}} = 183 \text{ km s}^{-1}$ . Our CO observations implied that most of the dense gas is concentrated in a few clumps with typical radius of 185 pc. The typical  $\text{H}_2$  mass of a high density component is  $\sim 3.0 \times 10^8 \text{ M}_\odot$ , which is about 10% of the dynamic mass assessed in the nuclear region ([5]). Given the fact that the optical depth of  $\tau_{\text{CO}(J=6-5)} = 3.9$ , the mass derived from the column density gives a lower limit on the total mass of the gas. If

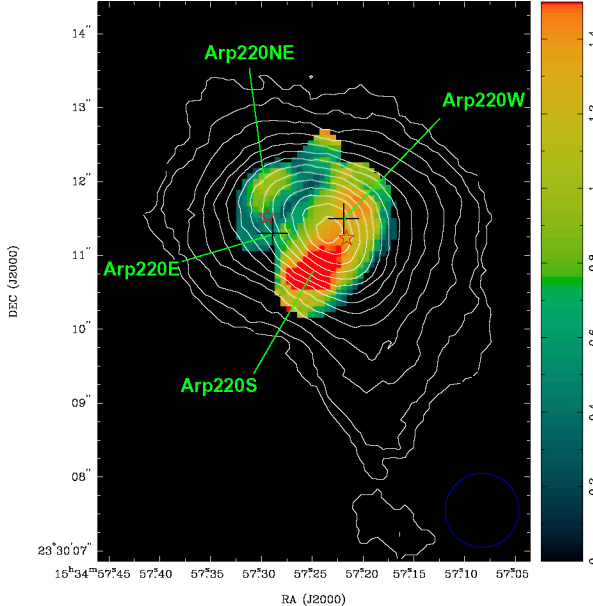


**FIGURE 5.** The intensity ratio map of  $^{12}\text{CO}$   $J=6-5/J=3-2$  lines (grey scale) overlapped with the  $^{12}\text{CO}$   $J=3-2$  velocity-integrated intensity (contours). The two line emission was restored with the same  $1'' \times 1''$  beam. The crosses show the positions of two radio nuclei. The red stars show the peaks of  $\text{H}33\alpha$  line emission [16]. Contour levels are  $20 \times 1, 2, 4, 6, 8, 10, \dots$   $\text{Jy beam}^{-1} \text{ km s}^{-1}$ . The grey scale covers the range 0–1.5 in line ratio.

the high density  $\text{H}_2$  gas distributes in a spherical volume with a radius of 185 pc, a density of  $n(\text{H}_2)=1.5 \times 10^5 \text{ cm}^{-3}$  and a filling factor of  $f_V = 0.01$ , the  $\text{H}_2$  mass of  $1.9 \times 10^9 \text{ M}_\odot$  is inferred.

The previous high-angular resolution observations of lower- $J$  CO[17, 5] suggested the presence of two counterrotating nuclear disks associated with the continuum cores of Arp220W and Arp220E. The molecular clouds might have been subject to inelastic collisions. A large fractional kinetic energy of the rotating disks might have transferred to the internal energy, heating the molecular clouds. The high density, warm components observed in  $\text{CO}(J=6-5)$  appeared to be a good evidence for the excitation of the higher- $J$  CO line transitions by inelastic collisions of molecular clouds.

Arp 220S and Arp 220NE are associated with the brightest CO ( $J=6-5$ ) emission. The concentration of a large bulk of dense and warm gas due to the consequence of inelastic collision might have enhanced the local star formation activity. However there has been no significant radio emission from these regions suggesting that they are probably the primeval regions for potential starbursts.

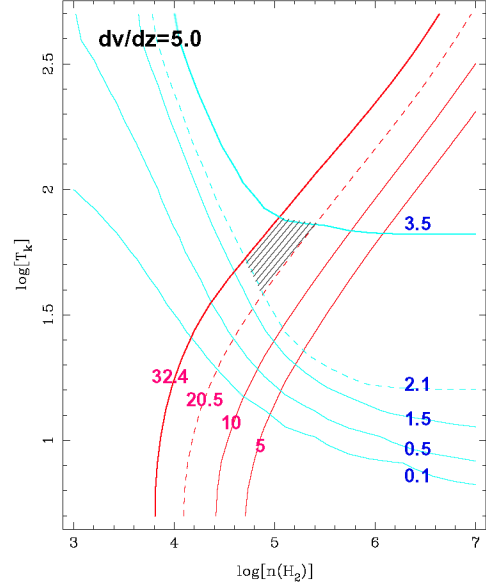


**FIGURE 6.** Results from the LVG model calculations: the curves of calculated ratio of the line intensity  $^{12}\text{CO}(J=2-1)/^{13}\text{CO}(J=2-1)$  with the values of 32.4, 20.5, 10 and 5 are plotted. The curves of  $\text{CO}(J=6-5)/\text{CO}(J=3-2)$  with values of 3.5, 2.1, 1.5, 0.5 and 0.1 are plotted. The dashed curves correspond to the observed values and the thick solid curves to the corrected values. The hatched region is the solutions for the excitation condition.

## STARBURSTS AT HIGH REDSHIFTS

At high redshifts, galaxy-galaxy collisions and mergers become common, triggering violent starbursts. The detailed observations of Arp220 have shown that the higher rotational  $J$  transitions can be excited via inelastic collision in the interface regions of the interactions between nuclear disks. Submillimeter observations of the higher  $J$  CO lines appear to be excellent probes to the star formation activities at high  $z$ .

## ACKNOWLEDGMENTS

The Submillimeter Array is a joint project between the Smithsonian Astrophysical Observatory and the Academia Sinica Institute of Astronomy and Astrophysics and is funded by the Smithsonian Institution and the Academia Sinica. Tao An was supported in part by NSFC (10503008, 10333020).

## REFERENCES

1. Anantharamaiah, K.R., Viallefond F., Mohan N.R., Goss W.M., & Zhao J.-H., 2000, ApJ, 573, 613–630
2. Arp, H., 1966, ApJS, 14, 1–20
3. Baan, W.A., & Haschick, A.D., 1995, ApJ, 454, 745–748
4. Bayet, E.; Gerin, M.; Phillips, T. G. & Contursi, A., 2006, A&A, 460, 467–485
5. Downes, D., & Solomon, P.M., 1998, ApJ, 507, 615–654
6. Flower, D. R., 2001, J. Phys. B: At. Mol. Opt. Phys. 34, 2731–2738
7. Frerking, M.A., Langer, M.D., & Wilson, R.W. 1982, ApJ, 262, 590–605
8. Goldreich, Peter & Kwan, John, 1974, ApJ, 189, 441–454
9. Graham, J.R., Carico, D.P., Matthews, K., Neugebauer, G., Soifer, B.T., Wilson, T.D., 1990, ApJ, 354, L5–L8
10. Greve, T.R., Papadopoulos, P.P., Gao Y., Radford, S.J.E., 2006, astro-ph/0610378
11. Güsten, R. Philipp, S. D., Weiβ, A. & Klein B., 2006, A&A 454, L115–L118
12. Joseph, R.D., & Wright, G.S., 1985, MNRAS, 214, 87–95
13. McKee, C. F., Storey, J. W.V., Watson, D. M., & Green, S., 1982, ApJ 259, 647–656
14. Norris, R.P., 1988, MNRAS, 230, 345–351
15. Pettpas, G. R. & Wilson, C. D., 2000, ApJ 538, L117–L120
16. Ridriguez-Rico, C.-A., Goss, W.M., Viallefond, F., Zhao, J.-H., Gomez, Y., Anantharamaiah, K.R., 2005, ApJ, 633, 198–204
17. Sakamoto, K., Scoville, N.Z., Yun, M.S., Crosas, M., Genzel, R., Tacconi, L.J., 1999, ApJ, 514, 68–76
18. Schinke, R., Engel, V., Buck, U., Meyer, H., Diercksen, G. H. F., 1985, ApJ 299, 939–946
19. Scoville, N.Z., Sargent, A.I., Sanders, D.B., Soifer, B.T., 1991, ApJ, 366, L5–L9
20. Scoville, N.Z., Yun, M.S., & Bryant, P.M., 1997, ApJ, 484, 702–719
21. Scoville, N.Z., Evans, A.S., Dinshaw, N., Thompson, R., Rieke, M., Schneider, G., Low, F.J., Hines, D., Stobie, B., Becklin, E., Epps, H., 1998, ApJ, 492, L107–L110
22. Soifer, B.T., Helou, G., Lonsdale, C.J., Neugebauer, G., Hacking, P., Houck, J.R., Low, F.J., Rice, W., Rowan-Robinson, M. 1984, ApJ, 283, L1–L4
23. Soifer, B.T., Neugebauer, G., & Houck, J. R. 1987, ARA&A, 25, 187–230
24. Solomon, P.M., Radford, S.J.E., & Downes, D., 1990, ApJ, 348, L53–L56